nature communications

Article

https://doi.org/10.1038/s41467-025-58731-4

# Temperature-triggered inflatable hydrogel muscles with snap-through instability for untethered robots

Received: 11 October 2024

Accepted: 28 March 2025

Published online: 10 April 2025

Check for updates

Yande Cui[1,2], Jianhua Hu[2], Ziyang Dong[2], Bing Li[1] ✉ & Chunyu Chang[1,2] ✉

Pneumatic artificial muscles have been widely used in the field of robotics because of their large output force and fast actuation, however, the accompanying bulky compressors and pumps limit their miniaturized applications. Despite current untethered pneumatic artificial muscles can be driven by adjusting the internal pressure, it is challenging to structurally mimic natural muscles with high water content. Here, we propose untethered pneumatic artificial muscles comprising a hydrogel actuator with snap-through instability and an air storage chamber. These hydrogel actuators can realize the conversion from hydrophobic association of octyl acrylate moieties to host-guest interaction between $\beta$-cyclodextrin and octyl acrylate under thermal stimuli, leading to the decrease of their moduli. The inflated hydrogel actuators exhibit rapid actuation with a radial expansion speed of 200% $s^{-1}$, which are powered by snap-through instability, thermal expansion of the gas inside the hydrogel actuator, and evaporation of water on its internal surface. With the pneumatic artificial muscles miniaturized, we demonstrate diving and rolling robots, exemplifying bionic robots able to adapt to and modify the environment. We expect that the design of hydrogel actuator in miniaturized pneumatic artificial muscles will facilitate rapid locomotion for future bionic robotic platforms.

Pneumatic artificial muscles (PAMs) have been widely used in the robotics industry because of their simplicity, flexibility, safety, and economy[1–6]. Traditional PAMs built from air bladders and braided sleeves were tethered for activation to components, such as compressors, pumps, and valves[7]. For example, McKibben muscles, invented for orthotics in the 1950s, changed length by inflating the inner bladders that were surrounded by the braided sheaths[8]. Despite PAMs possessing large output force and fast actuation speed, their portability and miniaturization applications were limited by the bulky peripheral components[9]. To develop untethered PAMs, two main strategies were adopted: generating the required pressure inside the pneumatic chamber[10] and expanding the muscle by using the principle of snap-through instability[11,12]. For the former strategy, some methods have been adopted to achieve actuation, including combustions[13], gas evolution reactions[14], swelling/deswelling,[15] and liquid-to-gas phase transition[16,17]. Among them, liquid–gas phase transition fluids have served as reversible pneumatic working mediums to generate required pressure, enabling pumpless control through magnetic, light, or thermoelectric stimulation[9,18–20]. The later strategy was to utilize snap-through instability of actuator, harnessing high-pressure gas to achieve rapid response and large volumetric expansion[11,21]. Soft actuators are bistable intrinsically because of their highly nonlinear pressure–volume relationship, similar to that of elastic balloons[12,22]. For example, untethered PAMs composed of dielectric elastomers could contract along the thickness direction and expand in the in-plane direction under voltage input[23], where a sudden

[1]Department of Urology, Zhongnan Hospital of Wuhan University, Wuhan 430070, China. [2]College of Chemistry and Molecular Sciences, Wuhan University, Wuhan 430072, China. ✉e-mail: bingli2023@whu.edu.cn; changcy@whu.edu.cn

decrease in pressure at a critical point triggered the snap-through instability[24].

To mimic muscles structurally, hydrogels had inherent advantages because they contained a large amount of water similar to human tissues[25–27]. Benefitting from the sophisticated design routes and diverse synthesis methods of hydrogels with excellent mechanical performances, the emerging hydrogel artificial muscles exhibited comparable deformability and work capacity with natural muscles[28–30]. However, hydrogel muscles are actuated based on polymer networks swelling and shrinking through the diffusion of water, a mechanism that makes actuation sluggish[31,32]. For example, hydrogels composed of polymers with an upper critical solution temperature will swell upon heating, whereas hydrogels composed of polymers with a lower critical solution temperature will shrink. These phase transition processes in hydrogels rely on the diffusion of water to cause changes in volume, which limits the speed of actuation. Recent advances in hydrogel-based PAMs enable rapid actuation and are employed in human-friendly interaction applications due to their adjustable compliance. However, there is still a bottleneck in the utilization of smart hydrogels to regulate air pressure instead of air pumps in wireless pneumatic actuators. To develop untethered artificial muscles with both tissue-like structure and rapid actuation speed, investigators have sought to integrate snap-through instability into hydrogel actuators. In this way, snap-through instability would be harnessed to all but instantaneously trigger large changes in internal pressure, resulting in fast expansion of the actuator. The rapid switching of the hydrogel modulus from hard to soft in response to external stimuli via a water diffusion mechanism became an issue. Therefore, developing PAMs using hydrogel-based actuators with snap-through instability remains challenging.

In this work, we presented a miniaturization strategy for obtaining untethered PAMs by inflating hydrogel actuators with snap-through instability and subsequently removing the peripheral compressor and pump after pressurizing (Fig. 1a). Typical pressure-volume curves of the hydrogel actuator at 20 °C and 70 °C are shown in Fig. 1b. The hydrogel actuator was pressurized to near the critical pressure at 20 °C (Stable state I), while the volume of actuator slightly increased. By heating to 70 °C, the modulus of the hydrogel actuator decreased through a thermal-induced phase transition, leading to a downward shift in the pressure-volume curve. At this point, the internal air pressure exceeded the critical pressure, triggering snap-through instability and leading the hydrogel actuator to rapidly expand into stable state II (Fig. 1c). The actuation of untethered PAM could be completed within 10 s at 70 °C, where the hydrogel actuator deformed from state I to state II with a radial actuation speed of 200% $s^{-1}$ (Fig. 1d and Movie S1). Furthermore, we also demonstrated the potential applications of these miniaturized PAMs in the fields of rapid biomimetic motions, including controllable diving devices and integrated rolling robots. Our design enables untethered PAMs to sense and modify their environment.

## Results

Since the untethered PAMs require hydrogel actuators possessing tunable elastic modulus as bladders, we designed thermally responsive hydrogels with switchable crosslinking. First, organogels were synthesized by polymerization of octyl acrylate (OA) and acrylamide (AAm) in the presence of $\beta$-cyclodextrin ($\beta$-CD), with *N,N'*-methylenebisacrylamide (MBA) and Irgacure 2959 as the crosslinker and initiator, respectively (Fig. 2a). After water exchanging, hybrid cross-linked $\beta$-CD/OA hydrogels were obtained, where the hydrogel network included chemical crosslinks, hydrophobic associations of alkyl chains (physical crosslinks), and randomly distributed $\beta$-CD. Because the formation of hydrophobic associations in hydrogel networks depended on the content of OA moiety, we investigated the influence of OA molar fraction on the assembly behavior and host-guest interaction between $\beta$-CD and P(AAm-*co*-OA) in the solvents (Fig. S1). When the OA molar fraction of $\beta$-CD/P(AAm-*co*-OA) was 6.7%, a transparent solution formed in water, due to the host-guest interaction between $\beta$-CD and OA. In the $^1$H NMR spectra of $\beta$-CD and P(AAm-*co*-OA), the characteristic peaks of H3 and H5 for $\beta$-CD shifted upfield, whereas the

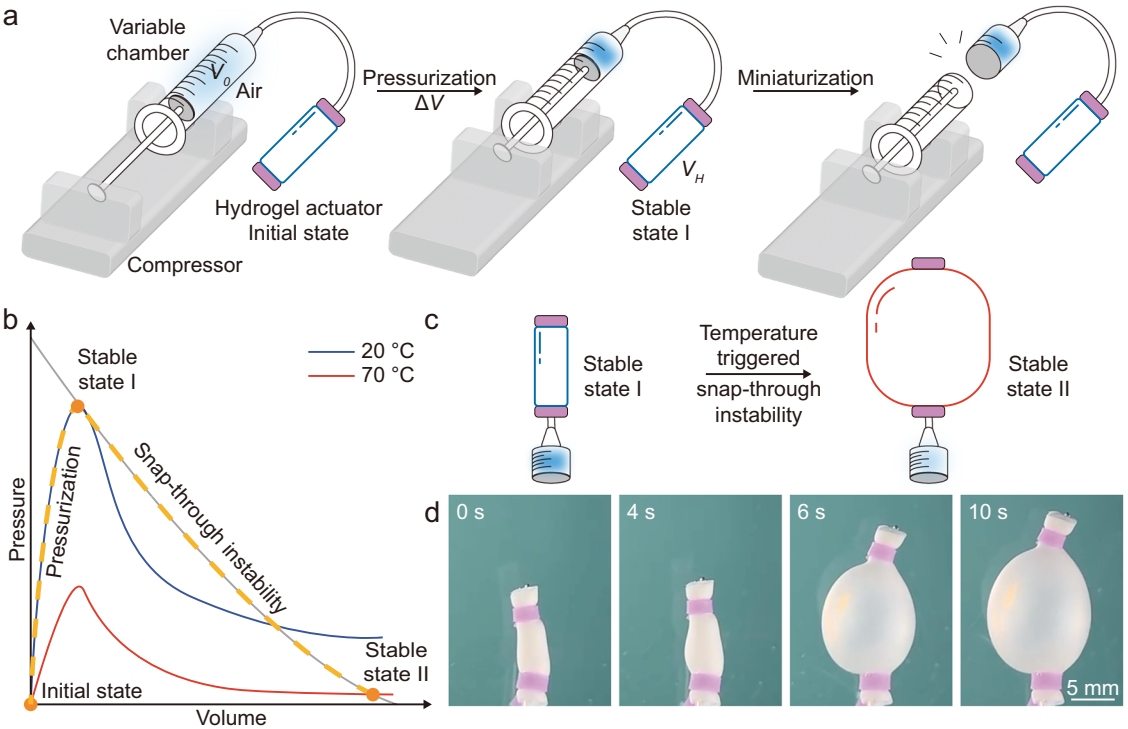


**Fig. 1 | Miniaturization design of the untethered PAM composed of hydrogel actuator. a** Schematic diagram of the design of the untethered PAM. **b** Typical pressure-volume curves of the hydrogel actuator with snap-through instability. **c** Temperature-triggered deformation of the inflated hydrogel actuator harnessing snap-through instability. **d** The actuation process of the inflated hydrogel actuator in 70 °C water.

https://doi.org/10.1038/s41467-025-58731-4

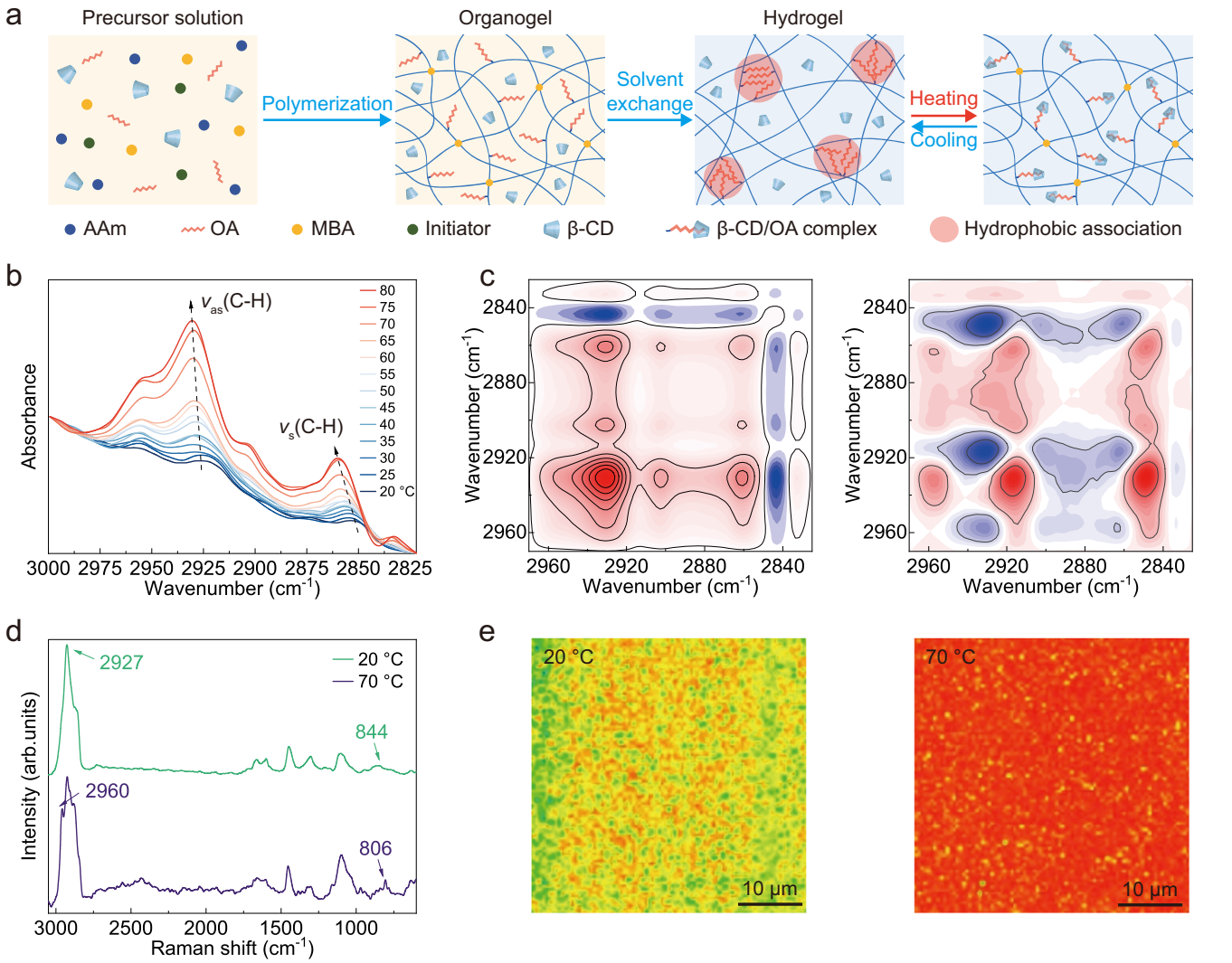


**Fig. 2 | Synthesis and characterization of *β*-CD/OA hydrogels. a** Synthesis and phase transition mechanism of *β*-CD/OA hydrogels. **b** Temperature-dependent ATR-FTIR spectra of *β*-CD/OA hydrogels. **c** Synchronous and asynchronous 2D correlation spectra of *β*-CD/OA hydrogels. **d** Raman spectra of *β*-CD/OA hydrogels at 20 and 70 °C. **e** 2D Raman images of the *β*-CD/OA hydrogels (Intensities of C–H stretching vibration modes).

characteristic peaks of OA side chains (methyl and methylene groups) on P(AAm-*co*-OA) shifted downfield, indicating the formation of host-guest interactions between alkyl chains and *β*-CD in water (Fig. S2). However, as the OA molar fraction was increased from 13.3% to 33.3%, P(AAm-*co*-OA) precipitated in water. These results indicated that P(AAm-*co*-OA) with high OA content formed stable hydrophobic associations instead of host–guest interactions.

To help understand the influence of OA molar fraction on the hydrogel networks, the appearance of *β*-CD/OA organogels before and after water exchange are shown in Fig. S3. As the molar fraction of OA increased from 6.7% to 26.7%, *β*-CD/OA organogels became transparent due to the high solubility of OA moiety in DMF. The *β*-CD/OA organogel with an OA molar fraction of 33.3% was translucent, which could be attributed to the high content of *β*-CD in polymeric networks. After water exchange, only the *β*-CD/OA hydrogel with an OA molar fraction of 6.7% was transparent, revealing the formation of host–guest interactions in hydrogel networks. As the molar fraction of OA increased from 13.3% to 33.3%, the hydrogels gradually became opaque, indicating that hydrophobic associations were dominant in hydrogel networks. To obtain hydrogels with a high modulus for inflation and then a reduced modulus after phase transition, the hydrogel needed to form at first a strongly hydrophobic crosslinked network after solvent exchange. During the exchange process, water permeated into organogel networks, resulting in the opaque appearance of hydrogels due to hydrophobic association among the OA moieties (Fig. S4).

To support the proposed phase transition behavior of *β*-CD/OA hydrogels, we performed temperature-dependent FTIR from 20 to 80 °C (Fig. 2b). We focused on the C–H stretching region of methylene groups in OA moieties, including symmetric ($\nu_s$) and asymmetric stretching vibrations ($\nu_{as}$). As the temperature increased, the spectral intensities of methylene groups gradually increased, while the peaks for $\nu_{as}$ (C–H) and $\nu_s$ (C–H) shifted from 2926 to 2930 cm$^{-1}$ and from 2853 to 2860 cm$^{-1}$, respectively. These results suggested that the hydrophobic associations among OA moieties converted into host-gust interaction between OA alkyl groups and *β*-CD. To extract further information about thermal-induced interaction changes in *β*-CD/OA hydrogel, we used two-dimensional correlation spectroscopy (2D COS). As shown in Fig. 2c, synchronous and asynchronous spectra were generated to reflect the synchronized and unsynchronized changes of intensities at two given wavenumbers, respectively.[33] According to Noda's judging rule[34], the responsive order of the OA moiety to temperature increase is $\nu_s$(C–H) (methylene groups in hydrophobic association, 2849 cm$^{-1}$) → $\nu_{as}$(C–H) (methylene groups in

hydrophobic association, 2916 $cm^{-1}$) → $\upsilon$(C−H) (methyl groups, 2955 $cm^{-1}$) → $\upsilon_s$(C−H) (methylene groups in $\beta$-CD/OA complex, 2857 $cm^{-1}$) → $\upsilon_{as}$(C−H) (methylene groups in $\beta$-CD/OA complex, 2929 $cm^{-1}$) (Table S1). This sequence revealed that the thermal-induced phase transition of the $\beta$-CD/OA hydrogel was driven by the dissociation of hydrophobic interaction.

The thermal-induced phase transition behavior was further evaluated by the Raman spectra of $\beta$-CD/OA hydrogels at different temperatures. As shown in Fig. 2d, a new characteristic peak of the methylene groups in OA moieties appeared at 2960 $cm^{-1}$ after heating from 20 °C to 70 °C, indicating that the chemical environment surrounding OA alkyl chain changed in hydrogel networks. Moreover, the broad peak for the breathing vibration of the glucopyranose ring at 844 $cm^{-1}$ shifted to a sharp peak at 806 $cm^{-1}$, indicating that the conformation of $\beta$-CD changed after the formation of the host-guest complex, and the vibration of $\beta$-CD in the hydrophobic cavity was restricted by the OA. In correlation mode, 2D Raman images of hydrogels showed that hydrophobic interactions (green regions) at 20 °C converted into host-guest interaction (red regions) at 70 °C (Fig. 2e). Moreover, the formation of $\beta$-CD/OA complex in hydrogel networks was confirmed by the appearance of an exothermic peak at 70 °C in the DSC curve (Fig. S5), because the host-guest interaction is an enthalpy-dominated binding reaction[35,36].

Unlike the actuation speeds of traditional upper critical solution temperature hydrogels are limited by the diffusion rate of water, $\beta$-CD/OA hydrogels underwent phase transition (from hydrophobic association to host–guest interaction) without water exchange, with water content being maintained at ~50 wt% during the heating process from 20 to 80 °C (Fig. S6). The rapid phase transition of $\beta$-CD/OA hydrogels could be observed in both water and oil at 70 °C (Fig. S7 and Movie S2). When the temperature increased from 20 to 70 °C, the appearance of hydrogel changed from opaque (microphase separation) to transparent (homogeneous state), indicating that the hydrophobic association converted to host–guest interaction in hydrogel networks.

The microphase separation structure of $\beta$-CD/OA hydrogels endowed them with high elastic modulus and tensile strength. After heating to 70 °C, the formation of $\beta$-CD/OA complexes reduced the cross-linking density of the hydrogel network, resulting in a sharp decrease in the elastic modulus. Therefore, $\beta$-CD/OA hydrogel exhibited superior flexibility at 70 °C in comparison to that at 20 °C (Fig. 3a). To increase the modulus gap of $\beta$-CD/OA hydrogels before and after heating, we used tunicate cellulose nanocrystals (TCNCs) as reinforcements to enhance the mechanical properties of hydrogels. As the TCNC content reached 0.25 wt%, the elastic modulus of $\beta$-CD/OA hydrogels increased from 0.27 MPa to 0.56 MPa due to the high elastic modulus and aspect ratio of TCNCs (Fig. 3b and Fig. S8a)[37]. On the other hand, the mechanical performance of $\beta$-CD/OA hydrogels also depended on the molar fraction of OA that determined the interaction of alkyl chains in hydrogel networks (Fig. 3c and Fig. S8b). When the molar fraction of OA was 6.7%, the elastic modulus of $\beta$-CD/OA hydrogels was only 0.015 MPa because the formation of host-guest interactions decreased the crosslinking density of hydrogel networks. As the molar fraction of OA increased to 26.7%, the gap in modulus before and after the phase transition of the hydrogel reached 0.42 MPa, which was attributed to the formation of a densified microphase separation structure at 20 °C. But as the OA molar fraction increased still further to 33.3%, the elastic modulus of hydrogels decreased to 0.34 MPa, due to the conversion of microphase separation to macroscopic phase separation in hydrogel networks.

As shown in Fig. 3d, a large porous structure (pore size: ~230 nm) could be observed on the surface of the hydrogel with an OA molar fraction of 6.7%, indicating a low crosslinking density. As the molar fraction of OA gradually increased to 13.3%, the pore size of hydrogel significantly decreased to ~63 nm, indicating increased crosslinking density (Fig. S9). As the molar fraction of OA exceeded 20%, the surface of hydrogel became dense and compact, which could be attributed to the formation of hydrophobic associations in hydrogel networks. Finally, at an OA molar fraction of 33.3%, the hydrogel apparently underwent a macroscopic phase separation, leading to a decay of the elastic modulus. Therefore, TCNC content of 0.25 wt% and OA molar fraction of 26.7% were selected for the preparation of $\beta$-CD/OA hydrogels, even though the hydrogel showed insignificant transparency at 70 °C (Fig. S3).

The stress-strain curves of $\beta$-CD/OA hydrogels under different temperatures are shown in Fig. 3e. The modulus of hydrogels decreased from 0.56 to 0.13 MPa when the temperature increased from 20 to 80 °C, indicating that the dissociation of hydrophobic interactions reduced the crosslinking density of hydrogel networks. The toughness of hydrogel reached a maximum of 1.24 MJ $m^{-3}$ at 70 °C (Fig. 3f), which is the actuation temperature selected in subsequent experiments. Finally, rheological results showed that both $G'$ and $G''$ values of hydrogel decreased as the increase of temperature and tan $\delta$ reached a maximum value around 70 °C (Fig. 3g), revealing the possibility of inflating the $\beta$-CD/OA hydrogel actuator through this thermal-induced softening process.

An inflatable $\beta$-CD/OA hydrogel actuator was obtained by pouring the precursor solution into a tubular mold for polymerization. To optimize the radial expansion of the hydrogel actuator, we first modulated the dimensions of the tubular actuator, including length and thickness. Axial and radial expansion strain–volume relationships of actuators with different lengths were investigated (Fig. S10). All actuators exhibited higher expansion strains in the radical direction in comparison to the axial direction, and the radial expansion strains significantly increased as the temperature rose from 20 to 70 °C, due to the low elastic modulus and high toughness of actuators at 70 °C. Similarly, actuators with different thicknesses exhibited the same expansion trend in both radial and axial directions at 20–70 °C (Fig. S11). According to the above results, we selected an actuator with a thickness of 0.9 mm and a length of 6 mm for further study, as its radial expansion strain was optimal for a given inflation volume.

To obtain inflatable PAMs, the relationship between the expansion behavior of the hydrogel actuators and the pre-pressurized volume ($\Delta V$, the volume of compressed air) was monitored. The strain–$\Delta V$ curves of the hydrogel actuators were *S*-shaped, indicating three stages of the hydrogel actuators during the pre-pressurization process (Fig. 4a). The hydrogel actuator hardly expanded at first, then expanded dramatically and eventually stabilized gradually. Corresponding to the pressure–$\Delta V$ curves, the hydrogel actuators generated slight expansion strains until $\Delta V$ reached critical pressures, at which point the hydrogel actuator expanded dramatically with the decrease of pressure after exceeding the critical pressure (Fig. 4b). To achieve rapid actuation of the hydrogel actuator switching between two bistable states, the actuator first needed to be pre-pressurized to a high-pressure stable state (stable state I) prior to the critical pressure. To achieve a high actuation strain of the hydrogel actuator, $\Delta V$ should be increased as much as possible, which requires a large $V_0$ value. However, when the $V_O$ value exceeded 6 mL, the hydrogel actuator ruptured soon after reaching the critical pressure.

Radial expansion strain–$\Delta V$ curves of hydrogel actuators ($V_0$: 6 mL) at different temperatures are shown in Fig. 4c. These results indicated that the radial expansion strains of hydrogel actuators increased with the increase in temperature, reaching a maximum of 347% at 70 °C. Moreover, we calculated the expansion volume ($V_H$) of the hydrogel actuator to establish the pressure-$V_H$ relationship at different temperatures (Fig. 4d). Initially, the change of pressure in the curves was linear with pre-pressurization of the hydrogel actuator. After reaching stable state I, the pressure declined, which was attributed to the expansion of the hydrogel actuator by harnessing the snap-through instability. The expansion principle of the hydrogel actuator started with pressurization at 20 °C to reach a high-pressure stable

https://doi.org/10.1038/s41467-025-58731-4

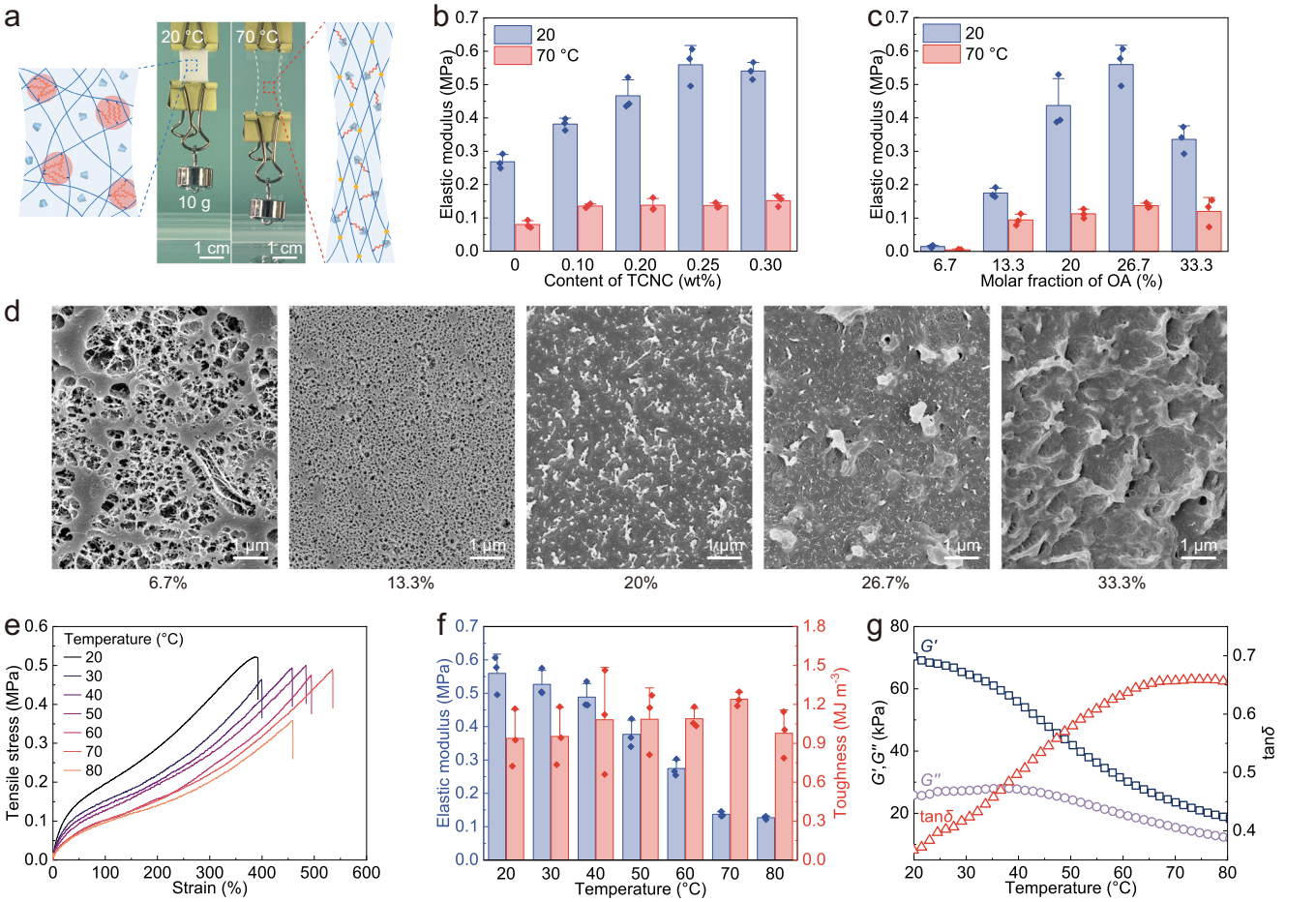


**Fig. 3 | Switchable mechanical properties of β-CD/OA hydrogel. a** Photographs and corresponding network structures of β-CD/OA hydrogel under 10 g load at 20 and 70 °C. **b** The elastic modulus of β-CD/OA hydrogel with different TCNC content and **c** molar fraction of OA. **d** SEM images of β-CD/OA hydrogel with different molar fractions of OA. **e** Stress–strain curves of β-CD/OA hydrogel under different temperatures. **f** Elastic modulus and toughness of β-CD/OA hydrogel under different temperatures. **g** The temperature dependence of storage modulus (*G′*), loss modulus (*G″*), and loss factor (tan *δ*) for β-CD/OA hydrogel. Note: for all boxplots, error bars represent standard deviation, $n = 3$ independent replicates.

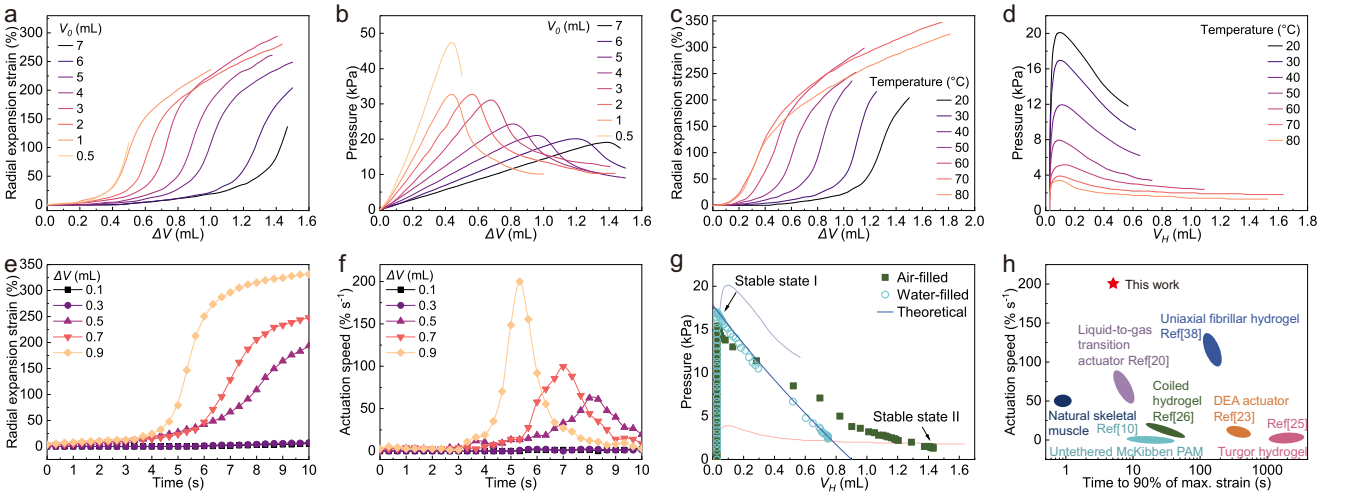


**Fig. 4 | Inflation and actuation performance of β-CD/OA hydrogel actuators. a** Radial expansion performance of hydrogel actuators with different initial chamber volumes ($V_0$). **b** Pressure changes in the inflation process of actuators at different $V_0$. **c** Radial expansion strain-Δ*V* curves of hydrogel actuators at different temperatures. **d** Pressure–volume ($V_H$, hydrogel volume) curves of hydrogel actuators at different temperatures. **e** Actuation kinetics of actuators inflating at 70 °C with different Δ*V*. **f** Actuation speed of hydrogel actuators inflating with different Δ*V*. **g** Pressure-volume and theoretical prediction curves of actuators when filled with air and water. **h** Actuation speed and time to reach 90% of the maximum strain compared to state-of-the-art untethered PAMs[10,20,23,25,26,38].

state close to the critical pressure, after which the actuator was separated from the pump and compressor. When the temperature was then increased from 20 to 80 °C, the critical pressure sharply decreased from 20.1 to 3.4 kPa, revealing that the elastic modulus of the $\beta$-CD/OA hydrogel could be switched by changing temperature. As the temperature increased to 70 °C, the pressure–$V_H$ curve shifted to a lower pressure level due to the decrease in modulus of the hydrogel. The pressure in the untethered PAM then exceeded the decreased critical pressure and triggered the snap-through instability, which caused the hydrogel actuator to expand until the pressure reached stable state II in the pressure–$V_H$ curve at 70 °C.

The inflated hydrogel actuators were capable of rapid expansion by harnessing the snap-through instability triggered at 70 °C. The actuation kinetics of the inflated hydrogel actuators with different $\Delta V$ are shown in Fig. 4e. The radial expansion strain of hydrogel actuators increased with the increase of $\Delta V$, while all curves of the hydrogel actuator were *S*-shaped (Fig. S12a), indicating that there was a rapid deformation stage during the actuation process corresponding to the peak of the actuation speed. The actuation speed of the hydrogel actuator significantly increased with increasing $\Delta V$ values (Fig. 4f). When $\Delta V$ was 0.9 mL, the actuation speed of the hydrogel actuator reached 200% $s^{-1}$. Since the pressure and volume of a given number of gas molecules in the system were inversely proportional, the pressure of the hydrogel actuator concomitantly decreased from 14.6 to 2.3 kPa within 10 s and finally stabilized at 1.3 kPa. (Fig. S12b). The relationship between the volume and pressure of the hydrogel actuator ($\Delta V$, 0.9 mL) during the expansion process is shown in Fig. 4g. The final $V_H$ of the hydrogel actuator was 1.43 mL, which was 50 times the initial $V_H$ (0.026 mL).

To clarify the actuation mechanism of our PAM, we compared the measured pressure–$V_H$ curve to the theoretical curve calculated by the ideal gas equation. We found that the experimental data deviated from the ideal gas equation, resulting in a larger final $V_H$. To explain this phenomenon, we hypothesized that the hydrogel actuator could be powered by both thermal expansion of the gas inside the actuator and evaporation of water from its internal surface of hydrogel actuator. To test this hypothesis, we conducted a control experiment by replacing the air in the hydrogel actuator with an equal amount of water and retaining the air in the chamber during actuation. In this case, the pressure–$V_H$ curve of the water-filled hydrogel actuator was consistent with the theoretical prediction, indicating that the expansion of the hydrogel was driven only by the snap-through instability. But in general, we should consider the thermal expansion of the air in the hydrogel actuator at 70 °C (1.17 times that at 20 °C). Therefore, the actuation of our PAM was driven by a combination of properties afforded by the hydrogel actuator; namely snap-through instability, thermal expansion of trapped air, and water evaporation from the inner surface.

The actuation speed and the time to reach 90% maximum strain of our PAMs were compared to those of natural muscles and reported works (Fig. 4h). Liquid-to-gas transition-based PAMs[20] and untethered McKibben PAMs[10] could complete the expansion and contraction, respectively, after more than ten seconds, but the actuation speed was limited by the lack of a bistable mechanism. The dielectric elastomer actuator exhibited bistable deformation under electrical stimulation, but the inherent viscosity of the dielectric elastomers limited their expansion speed under applied voltage[23]. In addition, the system required the connection of a chamber 5–10 times the volume of the actuator, restricting its integrated application. The solvent-responsive coil-shaped hydrogels showed large actuation strain, but their actuation speed was still limited by the permeation speed of solvent molecules[26]. The selectively permeable membrane enabled the turgor hydrogel a huge expansion actuation force, but was not conducive to the penetration rate of water molecules[25]. Uniaxial fibrillar hydrogel actuators improved actuation speed by reducing the permeation path of water (130% $s^{-1}$), which decreased sharply with the increase of swelling ratio, resulting in a great extension of the actuation time.[38] Although the actuation speed of natural skeletal muscles was lower than that of our hydrogel actuators, it took less time to complete the actuation because the actuation strain of the muscles was typically only about 20%. Benefiting from the combined effect of the snap-through instability, thermal expansion of the gas inside the actuator, and evaporation of water on the internal surface of the hydrogel actuator, our untethered PAM achieved an actuation strain speed of up to 200% $s^{-1}$. In addition, the compressibility and flowability of air enabled the hydrogel actuator to quickly equalize air pressure within the untethered PAM.

For the miniaturization of the untethered PAM, we reduced the volume of the air chamber ($V_0$) connected to the hydrogel. When $\Delta V$ was fixed at 0.3 mL, decreasing $V_0$ could significantly improve the actuation strain and speed of the hydrogel actuator (Fig. 5a). With $V_0$ of 1 mL, the radial expansion strain and the actuation speed of the hydrogel actuator reached 210% and 163% $s^{-1}$, respectively (Fig. S13). The actuation force of the hydrogel actuator at different expansion strains is shown in Fig. 5b. The blocking actuation force (Actuation strain: 0%) reached up to 0.45 N after heating for 3 s, and then the actuation force decreased with increasing expansion strain. Therefore, the untethered PAM with a $V_0$ of 1 mL enabled the miniaturization and integrated applications of the hydrogel actuator with a work capacity of 27.2 J $kg^{-1}$.

For applications, our miniaturized PAM consisted of a 3D-printed chamber (polyethylene terephthalate glycol, PETG) and a hydrogel actuator (Fig. 5c). The miniaturized PAM could expand and bend (assisted by strain-limiting optical fibers) rapidly in 70 °C water (Fig. 5d and Movie S3). One application we explored was to use the untethered PAM as a diving robot to detect water temperature by adjusting its buoyancy underwater (Fig. 5e and Movie S4). The diving robot quickly sank to the bottom once it was placed into 20 °C water due to the gravity it experienced being greater than its own buoyancy, and the resultant force was −1.5 mN. However, when placed in 70 °C water, the diving robot first sank to the bottom but then floated back up to the surface within 2 s, due to the thermal-induced expansion of the hydrogel actuator, and the resultant force increased to 3.2 mN. The miniaturized design made the gravity of the entire robot less than the buoyancy created by the expansion of the hydrogel, a buoyancy that overcame the limitation of bulky equipment such as compressors. The ability to regulate buoyancy enabled hydrogel actuators to be used in potential areas such as bionic fish, diving equipment, and underwater rescue. Another application we explored, inspired by the germination behavior of seeds that expand and push away soil and stones, we designed a rolling robot by using the untethered PAM. The rolling robot comprised an integrated chamber, wheels (PETG), and a hydrogel actuator with a total weight of 5 g (Fig. 5f). The expansion of the hydrogel actuator changed the position of the gravity center of the robot, resulting in a rolling motion. The hydrogel actuator could propel the rolling robot (140 times its own weight) forward 8.3 cm within 6 s under thermal stimulation (Fig. 5g and Movie S5). Our strategy gives intelligent robots a highly integrated architecture and environmental adaptability, enabling portable, miniaturized mobility and transportation.

## Discussion

In summary, we demonstrated an untethered pneumatic artificial muscle consisting of a hydrogel actuator with snap-through instability and an air storage chamber. The modulus of hydrogel networks significantly decreased *via* the thermal-induced phase transition, where the hydrophobic associations of OA moieties converted into host–guest complexes between $\beta$-CD and OA in hydrogel networks. The inflated hydrogel actuator rapidly expanded with a radial actuation speed of 200% $s^{-1}$ upon heating, which was driven by

https://doi.org/10.1038/s41467-025-58731-4

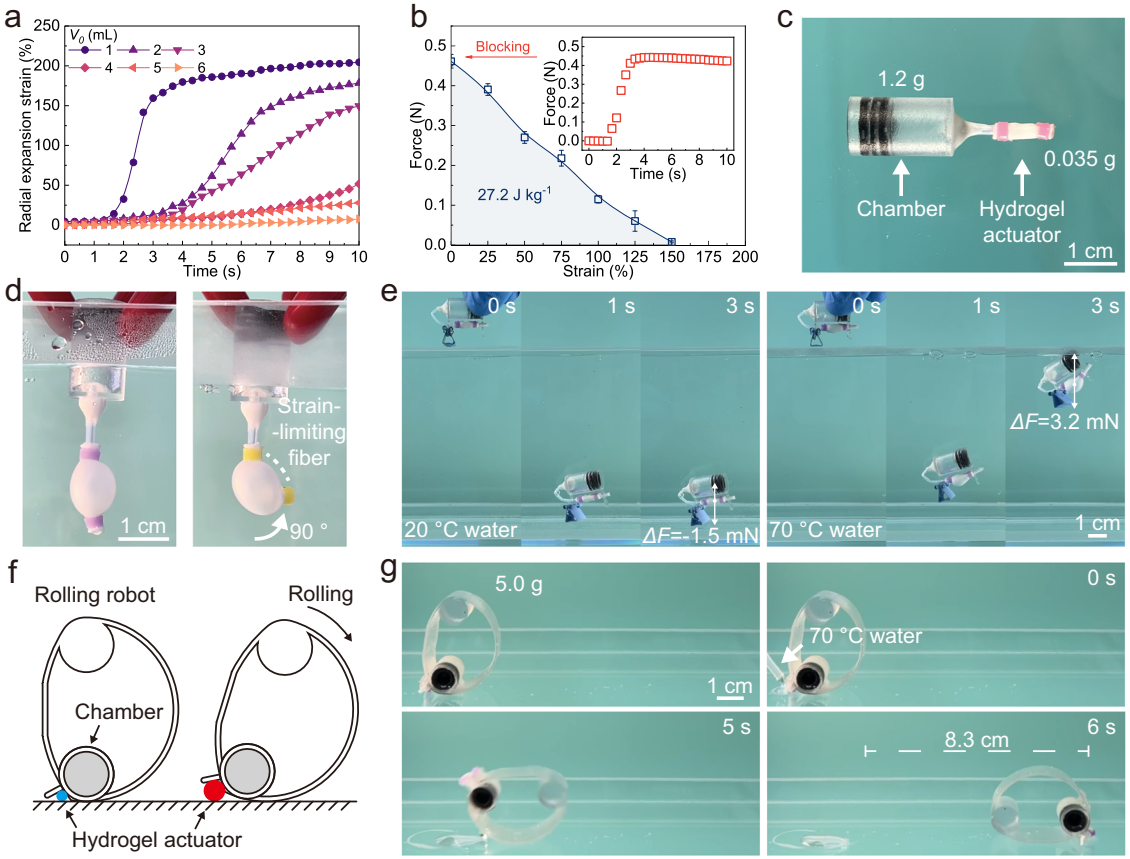


**Fig. 5 | Miniaturization and integrated applications of untethered PAMs.** **a** Actuation kinetics of miniaturized hydrogel actuator inflation at 70 °C with different $V_0$. **b** Actuation force of hydrogel actuator with different actuation strains. Error bars represent standard deviation, $n = 3$ independent replicates. **c** Untethered PAM consisting of a chamber and a hydrogel actuator. **d** The expansion and bending of the hydrogel actuator. **e** The diving robot sinking in 20 °C water and floating up in 70 °C water, respectively. **f** Schematic design of an integrated rolling robot. **g** Photographs of the rolling process of the robot triggered by 70 °C water.

snap-through instability, thermal expansion of the gas inside the actuator, and evaporation of water on the internal surface of the hydrogel actuator. After miniaturization, the untethered PAM could realize floating or rolling motion in response to temperature, suggesting their potential applications in the fields of diving or rolling robots.

## Methods

### Materials

*β*-cyclodextrin (*β*-CD, 98%), acrylamide (AAm, 99%) and octyl acrylate (OA, 98%) were purchased from Aladdin reagent Co. Ltd. *N,N*-dimethylformamide (DMF, 99%), *N,N'*-Methylenebisacrylamide (MBA, 98%), and (1-[4-(2-hydroxyethoxy)-phenyl]-2-hydroxy-2-methyl-1-propane-1-one) (Irgacure 2959, 98%) were purchased from Sinopharm Chemical Reagent Co., Ltd. Water was purified using an ultra-pure water system (SYS-III-10L, ShenYuan, China).

### Synthesis of *β*-CD/OA hydrogel

First, freeze-dried TCNC (0.002 g) was dispersed in DMF (0.8 g) to obtain a TCNC dispersion. Subsequently, *β*-CD (0.448 g), OA (82 μL), AAm (0.077 g), and MBA (0.012 g), as well as the prepared DMF solution of the photoinitiator Irgacure 2959 (20 wt%, 50 μL) were added to the DMF dispersion of TCNC (0.8 g, 0.25 wt%) to obtain a precursor solution. The precursor solution was injected into a transparent pipe mold with an inner diameter of 2 mm and an outer diameter of 5 mm. After being irradiated with 365 nm UV light for 3 h, the *β*-CD/OA organogel was obtained. Finally, after the organogel was immersed in water for three days, the *β*-CD/OA hydrogel was obtained.

### Characterization

The morphologies of *β*-CD/OA hydrogel were observed by field emission scanning electron microscopy (SEM) with a Zeiss SIGMA microscope (Zeiss, Germany) operated at 5 kV. The mechanical properties of *β*-CD/OA hydrogels were tested by using a universal testing machine (CMT6350, Shenzhen SANS, China) at room temperature with a tensile speed of 60 mm min$^{-1}$. Raman spectroscopy of *β*-CD/OA hydrogels was performed using a Raman imaging microscope (Thermo Fisher Scientific 5225 Verina Rd). Differential scanning calorimetry (DSC) analysis was conducted on the Q2000 apparatus from 10 to 80 °C with a heating/cooling rate of 10 °C min$^{-1}$ under $N_2$. FTIR spectroscopy of *β*-CD/OA hydrogels was recorded on a NICOLET 5700 FTIR spectrometer (Thermo Electron Scientific Instruments Corp., USA). Transmittance spectra of *β*-CD/OA hydrogels were evaluated by a double-beam UV-visible spectrophotometer (Mapada, China) from 300 to 800 nm. $^1$H NMR spectra of *β*-CD, P(AAm-*co*-OA), and *β*-CD/P(AAm-*co*-OA) were recorded on a 400 MHz NMR spectrometer (Avance-III, Bruker, Switzerland). The rheological behaviors of *β*-CD/OA hydrogels were evaluated on a DHR-2 rheometer (TA, USA) equipped with a parallel plate (Diameter: 40 mm) at a frequency of 0.5 Hz.

The actuation strain ($\varepsilon_{act}$) of *β*-CD/OA hydrogel actuators was calculated according to Eq. (1):

$$\varepsilon_{act} = (l_{act} - l_0)/l_0 \times 100\% \quad (1)$$

where $l_{act}$ was the radial or axial length of *β*-CD/OA hydrogel after actuation, and $l_0$ was the initial radial or axial length of *β*-CD/OA hydrogel.

The actuation work ($U$) was the area beneath the actuation force–strain curve, which was the work done by the radial expansion force. So, the work capity ($W$) of the hydrogel actuator was calculated by Eq. (2):

$$W = U/W_{H0} \tag{2}$$

where $W_{H0}$ was the initial mass of the hydrogel actuator.

The volume of the hydrogel actuator ($V_H$) was calculated by Eq. (3):

$$V_H = 4/3\pi(L/2)(D/2)^2 \tag{3}$$

where $L$ and $D$ were the length and diameter of the hydrogel actuator, respectively.

**Statistical analysis**. The data in the work were obtained through necessary transformation and normalization, where the outliers have been excluded through multiple experiments. Data are presented as mean ± standard deviation with sample size as indicated in the experiments. Statistical analysis was performed using Origin 2024.

## Data availability

The main data supporting the findings of this study are available within the article and its Supplementary Figs. The source data underlying Figs. 2–5, and Supplementary Figs. are provided as a Source Data file. Source data are provided with this paper. All data are available upon request. Source data are provided with this paper.

## References


1. Zhai, Y. C. et al. Desktop fabrication of monolithic soft robotic devices with embedded fluidic control circuits. *Sci. Robot*. **8**, eadg3792 (2023).
2. Morin, S. A. et al. Camouflage and display for soft machines. *Science* **337**, 828–832 (2012).
3. Gorissen, B. et al. Elastic inflatable actuators for soft robotic applications. *Adv. Mater*. **29**, 1604977 (2017).
4. Jones, T. J., Jambon-Puillet, E., Marthelot, J. & Brun, P. T. Bubble casting soft robotics. *Nature* **599**, 229–233 (2021).
5. Wang, Q. et al. Enhanced buoyancy and propulsion in 3d printed swimming micro-robots based on a hydrophobic nano-fibrillated cellulose aerogel and porous lead-free piezoelectric ceramics. *Nano Energy* **131**, 110254 (2024).
6. Wang, Y. et al. Moisture induced electricity for self-powered microrobots. *Nano Energy* **90**, 106499 (2021).
7. Li, M., Pal, A., Aghakhani, A., Pena-Francesch, A. & Sitti, M. Soft actuators for real-world applications. *Nat. Rev. Mater*. **7**, 235–249 (2022).
8. Higueras-Ruiz, D. R., Shafer, M. W. & Feigenbaum, H. P. Cavatappi artificial muscles from drawing, twisting, and coiling polymer tubes. *Sci. Robot*. **6**, eabd5383 (2021).
9. Ai, W., Hou, K., Wu, J., Long, Y. & Song, K. Miniaturized and untethered mckibben muscles based on photothermal-induced gas-liquid transformation. *Nat. Commun*. **15**, 2661 (2024).
10. Mirvakili, S. M., Sim, D., Hunter, I. W. & Langer, R. Actuation of untethered pneumatic artificial muscles and soft robots using magnetically induced liquid-to-gas phase transitions. *Sci. Robot*. **5**, eaaz4239 (2020).
11. Keplinger, C., Li, T., Baumgartner, R., Suo, Z. & Bauer, S. Harnessing snap-through instability in soft dielectrics to achieve giant voltage-triggered deformation. *Soft Matter* **8**, 285–288 (2012).
12. Overvelde, J. T., Kloek, T., D'Haen, J. & Bertoldi, J. K. Amplifying the response of soft actuators by harnessing snap-through instabilities. *Proc. Natl. Acad. Sci. USA* **112**, 10863–10868 (2015).
13. Bartlett, N. W. et al. A 3d-printed, functionally graded soft robot powered by combustion. *Science* **349**, 161–165 (2015).
14. Wehner, M. et al. An integrated design and fabrication strategy for entirely soft, autonomous robots. *Nature* **536**, 451–455 (2016).
15. Tondu, B., Emirkhanian, R., Mathé, S. & Ricard, A. A pH-activated artificial muscle using the mckibben-type braided structure. *Sens. Actuator A-Phys*. **150**, 124–130 (2009).
16. Mirvakili, S. M., Leroy, A., Sim, D. & Wang, E. N. Solar-driven soft robots. *Adv. Sci*. **8**, 2004235 (2021).
17. Wei, F., Zhai, Z. & Yang, L. Low-voltage-driven soft electrothermal actuators based on phase-change materials. *ACS Appl. Electron. Mater*. **5**, 5527–5536 (2023).
18. Yoon, Y. et al. Bioinspired untethered soft robot with pumpless phase change soft actuators by bidirectional thermoelectrics. *Chem. Eng. J*. **451**, 138794 (2023).
19. Lee, J. et al. Bioinspired soft robotic fish for wireless nnderwater control of gliding locomotion. *Adv. Intell. Syst*. **4**, 2100271 (2022).
20. Tang, Y. et al. Wireless miniature magnetic phase-change soft actuators. *Adv. Mater*. **34**, e2204185 (2022).
21. Chi, Y. et al. Bistable and multistable actuators for soft robots: Structures, materials, and functionalities. *Adv. Mater*. **34**, e2110384 (2022).
22. Ben-Haim, E., Salem, L., Or, Y. & Gat, A. D. Single-input control of multiple fluid-driven elastic actuators via interaction between bistability and viscosity. *Soft Robot* **7**, 259–265 (2020).
23. Hines, L., Petersen, K. & Sitti, M. Inflated soft actuators with reversible stable deformations. *Adv. Mater*. **28**, 3690–3696 (2016).
24. Baumgartner, R. et al. A lesson from plants: High-speed soft robotic actuators. *Adv. Sci*. **7**, 1903391 (2020).
25. Na, H. et al. Hydrogel-based strong and fast actuators by electro-osmotic turgor pressure. *Science* **376**, 301–307 (2022).
26. Cui, Y., Li, D., Gong, C. & Chang, C. Bioinspired shape memory hydrogel artificial muscles driven by solvents. *ACS Nano* **15**, 13712–13720 (2021).
27. Cui, Y. et al. Hydration programmable, shape memorable artificial muscles for antagonistic movements. *Adv. Funct. Mater*., 2401005 (2024).
28. Liu, X., Liu, J., Lin, S. & Zhao, X. Hydrogel machines. *Mater. Today* **36**, 102–124 (2020).
29. Mirvakili, S. M. & Hunter, I. W. Artificial muscles: mechanisms, applications, and challenges. *Adv. Mater*. **30**, 1704407 (2018).
30. Cui, Y. et al. Nanocellulose-based soft actuators and their applications. *J. Polym. Sci*. **62**, 280–296 (2023).
31. Tang, L. et al. Poly(n-isopropylacrylamide)-based smart hydrogels: design, properties and applications. *Prog. Mater. Sci*. **115**, 100702 (2021).
32. Yuk, H. et al. Hydraulic hydrogel actuators and robots optically and sonically camouflaged in water. *Nat. Commun*. **8**, 14230 (2017).
33. Ye, H., Wu, B., Sun, S. & Wu, P. Self-compliant ionic skin by leveraging hierarchical hydrogen bond association. *Nat. Commun*. **15**, 885 (2024).
34. Wu, J., Wu, B., Xiong, J., Sun, S. & Wu, P. Entropy-mediated polymer-cluster interactions enable dramatic thermal stiffening hydrogels for mechano adaptive smart fabrics. *Angew. Chem. Int. Ed*. **61**, e202204960 (2022).
35. Qu, X.-K. et al. Host–guest complexation of β-, γ-cyclodextrin with alkyl trimethyl ammonium bromides in aqueous solution. *J. Solut. Chem*. **36**, 643–650 (2007).
36. Yu, A. C. et al. Physical networks from entropy-driven non-covalent interactions. *Nat. Commun*. **12**, 746 (2021).
37. Peng, N. et al. Controlled arrangement of nanocellulose in polymeric matrix: From reinforcement to functionality. *ACS Nano* **14**, 16169–16179 (2020).

38. Benselfelt, T., Rothemund, P. & Lee, P. S. Ultrafast, high-strain, and strong uniaxial hydrogel actuators from recyclable nanofibril networks. *Adv. Mater.* **35**, e2300487 (2023).

## Acknowledgements

C.C. wishes to thank the National Natural Science Foundation of China (52073217 and 52373104). The authors thank Dr. Tobias Baskin from the University of Massachusetts Amherst for the language editing of this paper.

## Author contributions

Y.C. and C.C. conceived the idea and designed the experimental protocol. Y.C. performed and completed the entire experimental study. J.H. and Z.D. provided the necessary experimental help. Y. C. organized the Figures and wrote the draft. B.L. gave technical suggestions. Y.C. and C.C. revised and finalized the paper.

## Competing interests

The authors declare no competing interests.

## Additional information

**Supplementary information** The online version contains supplementary material available at https://doi.org/10.1038/s41467-025-58731-4.

**Correspondence** and requests for materials should be addressed to Bing Li or Chunyu Chang.

**Peer review information** *Nature Communications* thanks the anonymous reviewer(s) for their contribution to the peer review of this work. A peer review file is available.